



Supplementary Materials for

Constraints on the Late Holocene Anthropogenic Contribution to the Atmospheric Methane Budget

Logan Mitchell,* Ed Brook, James E. Lee, Christo Buizert, Todd Sowers

*Corresponding author. E-mail: Logan.E.Mitchell@gmail.com

Published 22 November 2013, *Science* **342**, 964 (2013)

DOI: 10.1126/science.1238920

This PDF file includes:

Materials and Methods
Figs. S1 to S17
Tables S1 and S2
References

Materials and Methods

1.) Analytical Methods

1.1) Sample measurement

Air was extracted from ice core samples using a wet extraction technique, and the methane concentration was measured with a gas chromatograph (GC) using techniques that have been described in detail elsewhere (1-3). Briefly, a ~10 cm tall slab of ice was divided into two samples each with a cross sectional area of ~2.5 cm x 2.5 cm. The outer 1-2 mm of the sample was trimmed with a bandsaw yielding an average sample mass of 60.5 g. Samples were then placed in a pre-chilled glass flask with a glass to metal transition and Conflat flange and sealed to the extraction line with a copper gasket. While on the extraction line the flasks were submerged in a chilled ethanol bath maintained at -70°C. Ambient air was pumped from the flasks for one hour using a turbo molecular pump, and the samples were melted by submersion of the flasks in a hot water bath, releasing the air from the ice into the flask headspace. The flasks were then re-submerged in the ethanol bath to freeze the sample and lower the water vapor pressure in the headspace. The air from each flask was expanded into the sample loop of a GC equipped with a flame ionization detector four times and the concentrations were averaged. The mean values for each pair of samples were averaged to produce a mean concentration for each depth (Fig. S1).

The methane concentrations were then calculated using a linear regression line fitted to the peak area over pressure from a working air standard (500.2 ppb methane on the NOAA04 methane scale (4)). The concentration of the working air standard was periodically calibrated to primary laboratory standard tanks with concentrations ranging from 380 to 1853 ppb, which were in turn calibrated by the NOAA GMD Carbon Cycle Group on the NOAA04 methane scale.

In the summer of 2009 the extraction line was rebuilt to increase the throughput from 8 samples per day to 12 samples per day. In the fall of 2010 foam insulation was added around the bath and extraction line which reduced the thermal gradient inside the flasks and decreased the blank corrections of the rebuilt extraction line by ~2 ppb, otherwise the apparatus has remained unchanged.

Methane concentrations were measured from 1,616 individual ice core samples from 709 discrete depths. Of these, 291 sample depths (644 individual samples) were from the Greenland Ice Sheet Project 2 (GISP2, 72.6° N, 38.5° W) ice core covering 811 B.C.E. to 1824 C.E. yielding a mean sampling resolution of 11 years. There is a gap from 708 C.E. to 785 C.E. as no ice was available between 345-359 m. 400 sample depths (902 individual samples) were from the WAIS Divide deep ice core (WDC06A, 79.4676°S, 112.0865°W) covering 2,604 B.C.E. to 1783 C.E. The WDC06A record was combined with data from 18 sample depths (38 individual samples, 14 of which were previously published (1) and 24 were new) from the WDC05A shallow ice core from 1784-1909 C.E. to yield a complete WAIS Divide record covering 2,604 B.C.E. to 1909 C.E. with a combined mean sampling resolution of 11 years. 44 sample pairs (11 pairs from WDC06A and 33 pairs from GISP2, 5% of the total number of samples) were rejected because of problems with the extraction line, leaks, extreme disagreement between replicates (>4 standard deviations), and samples with cracks in the ice. 11 GISP2 sample depths (32 individual samples) were excluded due to suspected in-situ methane production, discussed in detail below. The pooled standard deviation of the pairs of samples measured on the same day is 2.0 ppb (excluding the rejected measurements). All of these data are plotted in Fig. S1.

To establish the analytical precision, duplicate pairs of samples from 98 sample depths (47 from GISP2 and 51 from WAIS Divide) were measured. The pooled standard deviation between duplicate pairs of samples is 2.4 ppb. This is slightly higher than the pooled standard deviation between pairs of samples because it incorporates the additional uncertainty from slight changes in day-to-day procedures, solubility, and blank ice corrections. This was taken as the best estimate of the 1σ uncertainty of the complete data set.

1.2) Blank correction

To constrain the influence of leaks or other contamination, air-free ice (AFI, see Mitchell et al. (2011) for a description of how AFI was produced) was routinely measured. Sample preparation and analysis with AFI was identical to that of typical samples except that after ambient air was pumped out of the flasks the working standard was added over the AFI to a pressure of ~50 torr. Average AFI corrections were linearly interpolated between days when AFI was analyzed to create a time-dependent correction. Occasionally, AFI was measured along with real ice core samples and in those cases the mean AFI concentrations from that day was used to correct the samples instead of interpolated values. The mean and standard deviation AFI correction to the data is 2.5 ± 1.6 ppb.

1.3) Gravitational fractionation correction

Within the firn, gasses undergo a mass dependent fractionation due to gravity (5-7). The magnitude of this fractionation is controlled by the thickness of the diffusive column of the firn. Since the isotopic composition of atmospheric N_2 ($\delta^{15}N$) has remained constant over timescales relevant to ice cores (8) the measured $\delta^{15}N$ was used to correct for this gravitational fractionation. Methane ($M = 16.04 \text{ g mol}^{-1}$) is fractionated relative to dry air ($M = 28.96 \text{ g mol}^{-1}$) and the gravitational fractionation is therefore $\Delta M \times \delta^{15}N$. Linear interpolation between $\delta^{15}N$ measurements from both the WAIS Divide ice core (Severinghaus, J., personal communication, 2012) and the GISP2 ice core (9) were used to obtain $\delta^{15}N$ values at the depths of the methane samples. The mean correction factor for WAIS Divide samples is 1.00397 ± 0.00007 and for GISP2D is 1.00396 ± 0.00008 .

1.4) Solubility correction

When air is exposed to liquid water, a portion of it dissolves into the water in a ratio that is described by Henry's Law. While methane has about the same solubility as oxygen, it is ~2.5x as soluble as nitrogen and therefore the headspace methane concentration decreases during the procedure when the air was exposed to the melting sample water. Mitchell et al. (2011) empirically determined a methane solubility correction factor of 1.0170 ± 0.0031 for the extraction line used here.

2.) In-situ methane production in the GISP2 ice core.

A number of the GISP2 samples had methane concentrations elevated relative to both nearby samples and to values expected based on the WAIS Divide record (with a constant IPD added). For five depths enough ice was available to make a second measurement on a different day. In all cases good agreement was obtained between both days, confirming that the measurements represent the real concentration of methane in the ice. To investigate the possibility that these signals represent extremely abrupt atmospheric events, additional samples close to the elevated samples were measured (usually within about ± 1 m, corresponding to ± 5

years). No similarly elevated values were found in these nearby samples. Because the firm air diffusion and bubble trapping processes act as a smoothing filter of the atmospheric signal on the order of 20-40 years, it would be impossible for these single-point elevated values to represent real atmospheric events. It was therefore tentatively concluded that the elevated methane levels must have been the result of in-situ methane production, probably by microbial metabolism (10). To objectively identify which samples contain elevated concentrations we followed the approach of Schilt et al. (2010) who used a spline fit to the data to identify samples containing in-situ production of N₂O. This was better suited than a lowpass filter because it could be created using the raw time series data while a lowpass filter would require evenly spaced (interpolated) data. The Matlab function “csaps” with a smoothing parameter (p) of 0.011, roughly equivalent to a lowpass filter with a cutoff frequency of 3 years (12), was used to smooth the data. The sample with the highest elevation above the spline fit was identified and excluded, then the spine was refit, and this process was repeated until there were no samples which were elevated more than 2 σ (4.8 ppb) above the spline fit. This procedure identified 11 points which are shown in Fig. S2 along with the final spline fit.

Correlations between the elevated methane concentrations and trace element chemical records from GISP2 (13) were examined to search for a possible source of in-situ methane production by microbial metabolism. Some, but not all, of the samples with elevated methane concentrations also had elevated concentrations of ammonium (NH₄⁺). There is no notable correlation between methane artifacts and any other chemical species. This analysis was severely limited, however, by the fact that the GISP2 chemistry data generally had a ~44 cm sample resolution, whereas the samples presented here were 10 cm long and abrupt changes in chemistry can occur on centimeter scales at this depth range (13). In a few selected areas high-resolution (2 cm) chemical analysis was performed (13). One of these high-resolution chemical transects overlapped the methane sample at 583.6-583.7 m that has the largest methane spike (elevated ~70 ppb over nearby samples and the spline fit) and revealed a very large spike in NH₄⁺ in the middle of the methane sample. The low-resolution NH₄⁺ record shows a concentration of 43.9 ppb in a 40 cm long sample whereas the high-resolution NH₄⁺ record shows peak concentrations of 154 ppb and 78 ppb in two 3 cm long samples located in the middle of the depth interval encompassing the methane sample and lower concentrations (~5 ppb) surrounding. After making the initial measurement the remaining ice from this depth in the ice archive at the National Ice Core Laboratory was examined and was found to contain a ~2 cm thick cloudy band at the same depth of the high-resolution NH₄⁺ peak (Fig. S3). The origin of this cloudy band is uncertain. Although these observations offer compelling evidence for organic based in-situ production, it was not possible to unambiguously determine the cause.

Recently Rhodes et al. (2013) used continuous flow analysis of methane and trace elements on the NEEM S1 ice core from NW Greenland to examine these relationships in greater detail. They observed reproducible, abrupt, high amplitude methane spikes that could not have been atmospheric in origin. This study also observed that these spikes were closely associated with black carbon, NH₄⁺, and NO₃⁻, but they did not have a consistent relationship with inorganic chemical species derived from mineral dust. Since the NEEM S1 core is located ~650 km northwest of GISP2 it is possible that these methane spikes were the result of a widespread event which deposited the organisms and trace elements which were necessary for in-situ methane production over a large portion of the Greenland ice sheet. This hypothesis should be examined as other ice cores from Greenland are analyzed in greater detail in the future.

These observations raised the possibility that methane could be produced in-situ throughout the core, not only in the isolated areas discussed previously. This would have elevated the baseline methane concentration and also the methane IPD. This was highly unlikely for two reasons. First, microbial CH₄ production would require the simultaneous presence of both methanogenic microbes as well as nutrients, the deposition of which has a very high temporal variability associated with northern hemispheric weather events and seasonal patterns (Fig. S2) (13). Since the magnitude of suspected in-situ methane production is 7-70 ppb, if it was present it would be expected that the contamination would have obscured the multidecadal variability of methane which has a magnitude of 10-40 ppb. However the multidecadal scale variability is similar in both the GISP2 and WAIS Divide records as could be seen in the very high correlation coefficient between the bandpass (pass band = 20-100 years) filtered methane records ($r^2 = 0.85$). Second, if the small amplitude, high frequency trace chemical variations were causing smaller in-situ contamination (< 7 ppb) the high frequency variability of the GISP2 methane record would be larger relative to the WAIS Divide record. However, the standard deviation of the high pass (high pass cutoff = 5 years) filtered records is similar between the ice cores (GISP2 = 1.4 ppb, WAIS = 1.7 ppb).

Given these observations, the only possible type of in-situ production that could have been affecting the GISP2 record would be a small, constant amount of methane production throughout the core. Since microbial metabolism is the only hypothesized source of in-situ methane production and since this source would depend on the highly variable trace chemical deposition on the surface of the ice sheet, a small, constant amount of methane production throughout the core would be highly improbable. The ultimate confirmation that Greenlandic ice core records do not contain methane concentrations elevated by a small amount awaits a new Greenlandic ice core with a high enough accumulation rate to overlap the northern hemispheric record of direct atmospheric methane measurements, which began in 1983.

3.) Chronologies

To construct the IPD, the chronologies of both ice cores needed to be synchronized. The multidecadal events observed in both ice core records must have occurred simultaneously since the durations of the events were much larger than the atmospheric mixing time (~1 year). One ice core record was therefore taken as a “reference” and then a wiggle matching technique was used to obtain an optimal match based on the multidecadal variability – this works provided that the offset between the initial independent chronologies of both cores was smaller than the duration of multidecadal methane variations used in the synchronization.

A coupled heat diffusion-firn densification model was used to determine the ice age-gas age difference (Δ age) in the WAIS Divide and GISP2 ice cores. Accumulation rates were reconstructed for each core using measured annual layer thickness records with a simple 2-D ice flow model to correct for strain due to ice flow (15, 16). GISP2 temperatures were obtained from Kobashi et al., (2011); WAIS temperatures were based on a combination of the borehole temperature record and stable water isotopes (18, 19). Modern day CO₂ Δ age values of 205 and 190 years for WAIS and GISP2, respectively, were determined using firn air sampling data from WAIS and Summit stations (20-22). Because methane diffuses more quickly through the firn column than CO₂ does, two years were added to the modern day (CO₂ based) Δ age estimates (23). The firn densification model was a dynamical version of the Herron and Langway model (24) using ice thermal properties (25). $\delta^{15}\text{N}$ data was used to verify that the firn column thickness predicted by the densification model was correct.

These chronologies were used as starting points for an iterative Monte Carlo analysis which maximized the correlations between the bandpass filtered GISP2 and WAIS Divide records. The WAIS Divide layer counted chronology was probably more accurate as it was based on a combination of multi-parameter high-resolution chemistry records and electrical conductivity measurements. Therefore the WAIS Divide chronology was chosen to be the “reference” chronology and the GISP2 record was tied to the WAIS Divide record.

The iterative Monte Carlo procedure was conducted as follows. Step 1: Tie points between the methane records were chosen with an equal spacing of 200 years. Step 2: The following procedure was performed 1000 times: the depth of the tie points (standard deviation of 4 m, equivalent to ~20 years) were randomly perturbed to produce a new depth-age scale, a bandpass filter was applied to the records (passband of 20-100 years), and the correlation coefficient was calculated for the whole record. Each tie point therefore had 1000 results consisting of the depth and the correlation of the whole record. Step 3: The mean tie point depth of the 20% of records with the highest correlation coefficients was chosen. Step 4: Steps two and three were iterated through 50 times, which allowed the Monte Carlo procedure to converge on stable depth-age values for GISP2. However, individual iterations still contained small differences, so for Step 5 the mean depth of the final 25 iterations was taken. Step 6: The tie points were shifted by 20 years and steps one to five were performed again. Step six was repeated until 10 independent chronologies consisting of tie points that were spaced 200 years apart were created. Step 7: The 10 independent chronologies were combined into one final chronology. This final chronology is shown in Fig. S4 along with colored symbols that correspond to the 10 individual chronologies.

Two sensitivity tests demonstrate the robustness of the final combined chronology. First, using the GISP2 chronology as the “reference” chronology gives equivalent results. Second, timescales constructed with tie points spaced every 50 and 100 years tested the choice of 200 year tie point spacing. The closer spacing allowed the procedure to over fit the data and create very large oscillations in Δ age which are unrealistic. These sensitivity tests demonstrate that 1) the method of establishing the chronology yielded closely spaced tie points which provide detailed information about Δ age variability and 2) the 200 year tie point spacing of the individual component timescales prevented the procedure from over fitting the data.

The methane synchronized chronology provides an independent check for the accuracy of the original chronologies (Fig. S4). The methane synchronized GISP2 chronology is 0 ± 11 years different from the gas chronology found from by employing the dynamic firn model and the Meese/Sowers layer counted ice chronology (26). This offset is well within the estimated uncertainty of the layer counting (± 25 years) and firn densification modeling (± 20 years).

4.) Comparison with other ice core records

The new high-resolution records presented here compare well with previous high-resolution methane records from WAIS Divide (WDC05A) (1) and Law Dome (27, 28) (Fig. S1). The WDC05A shallow ice core was drilled at WAIS Divide ~1.3 km away from the main borehole (WDC06A) in the 2005/2006 drilling season. This core was drilled to a depth of 298 m (gas age ~1000 CE) without drilling fluid. For this comparison the WDC05A samples were plotted using the chronology for WDC06A since the two ice cores show nearly identical methane concentrations on a depth scale, indicating that there is little difference in age scales (1). The WDC05A record has a similar temporal resolution as the WDC06A record and excellently

reproduces the variability. Over the time period with data for both ice cores (1002-1780 CE) the correlation coefficient after linear interpolation between the mean of each sample is $r^2 = 0.92$.

The Law Dome ice core was drilled on the coast of Antarctica (66.733°S, 112.833°E) and since there are essentially no methane emissions in the high latitude Southern Hemisphere (SH) the atmospheric history derived from both cores should be the same (29). In reality there may be slight differences owing to different smoothing from diffusion in the firn and bubble trapping processes, but the differences between Law Dome and WAIS Divide shouldn't be large since both sites have a moderate to high accumulation rate. Overall there is excellent agreement between the WAIS Divide and Law Dome records after ~900 C.E. (Fig. S1, all records are on the NOAA04 calibration scale (4)). Mitchell et al., (2011) noted that the largest discrepancy between the WDC05A and Law Dome record over the past 1000 years is the multidecadal event from 1410-1470 C.E. which has a 10-15 ppb larger magnitude in the Law Dome record than the WDC05A record. The WDC06A and GISP2 records both confirm the magnitude of the event seen in the WDC05A record and suggest that the data for the three samples comprising this event in the Law Dome record may have been elevated. Between 0-900 C.E. the Law Dome record diverges from the WDC06A record; however it appears that this is due to a shift in the chronology. There is a large oscillation in the Law Dome record at ~300-500 C.E. that would match the WAIS Divide record if it was shifted ~80 years (Fig. S1).

5.) Monte Carlo Error Analysis of the IPD

To determine error bands around the IPD record a Monte Carlo analysis which incorporates the 1σ analytical measurement uncertainty of ± 2.4 ppb and a temporal uncertainty of ± 5 years for each of the tie points that were used. The measurements and the tie points were randomly perturbed 1000 times and then a lowpass filter with a cutoff frequency of 20 years was used to smooth each of the 1000 perturbed records. The standard deviation of the 1000 perturbed records was taken to obtain the uncertainty through time. The average 1σ uncertainty for the IPD was ± 3.3 ppb, as indicated with the grey shaded area in the figures plotting the IPD.

6.) Comparison with previous IPD estimates

Previous estimates of the IPD during the LPIH are shown in Fig. S5 (27, 30, 31). The four reconstructions are consistent with each other within their reported error bounds. The additional variability seen in the Etheridge et al., (1998) IPD data was probably caused by their Greenland sampling aliasing the multidecadal scale variability.

7.) Model description

To model the methane budget, an Eight Box Atmospheric Methane Model (EBAMM) was used. This model consists of six tropospheric boxes covering 30° latitude each and one stratospheric box in each hemisphere with the tropopause located at ~200 hPa (Fig. S6). This model was chosen because it can resolve the latitudinal distribution of methane emissions yet is simple enough to model methane concentrations over thousands of years using a personal computer. The original structure of EBAMM was developed in Simulink and was called BOSPAGE-8 (8-BOX SF₆ CALibrated Global Euler transport model) (32). This original model was reprogrammed and optimized for use in Matlab but it retained the original box structure, transport terms, and sink characteristics from BOSPAGE-8.

Each EBAMM box contains a constant mass of air and the molar ratios of methane isotopologues were changed by the sources, sinks, and transport between the boxes. Since the

present work focused on long term variations of methane, seasonal variability in the sources was not used. Atmospheric transport between the boxes was calibrated against modern SF₆ observations using singular value decomposition (SVD) and the interhemispheric transport was set to 1.67 years (32). A sensitivity test was performed to determine if the modeled IPD was sensitive to this interhemispheric transport parameterization. The test used the “N2+A1” emissions scenario (described below) but with a reduced interhemispheric transport time of 1 year, which would represent a very large change in interhemispheric transport. This reduced the IPD by 2.5 ppb demonstrating that the modeled IPD is not overly sensitive to the interhemispheric transport parameterization. The sink distribution and isotopic fractionation factors from OH and soil uptake were taken from BOSCAGE-8 and were originally taken from the 3D model (TM2) (33). In addition a self-feedback was incorporated into the sink term of 10% after Hopcroft et al., (2011). This caused a 100% change in source strength to yield a 110% change in concentration. The late Holocene changes in temperature, humidity, and volatile organic compounds (VOCs) were not large and it was assumed that their impact on OH could be neglected over this time period. The lifetime of methane was set to 10 years at 1500 C.E. A discussion of the implications of using a lifetime of methane of 8 or 12 years based on recent research (35) is in section 9 below.

The detailed source scenarios and changes through time are described below. Unless otherwise noted, the natural sources have latitudinal distributions that remained constant throughout the model runs and are listed in Table S1. The parameterization of anthropogenic emissions will be described in section 8.3.3. The modeled distribution of sources compares well with more complex models of the pre-industrial latitudinal distribution of sources from Harder et al., (2007) Fig. 2b, and also with zonal concentrations modeled in Kaplan et al., (2006) Fig. 8. Furthermore, the conclusions of this work are not sensitive to slight changes in the baseline latitudinal distribution of sources within reasonable limits.

Since EBAMM simulates atmospheric methane concentrations, the concentrations from Boxes 1 and 6 were passed through firn air smoothing filters to represent the smoothing of the atmospheric signal through the upper layer of the ice sheet known as the firn (e.g. (38, 39)). The firn air filters were determined with a firn air transport model and are shown in Fig. S7. The firn air model was calibrated using firn air measurements of reference tracers with known atmospheric history at WAIS and Summit, Greenland. Summit was chosen to represent GISP2 since there were many more firn air measurements from Summit and since Summit is only ~28 km away from GISP2 and should therefore have similar characteristics. Since this work is focused on changes in methane concentrations which occur on a much longer timescale than the width of the firn smoothing filters, the details of the filters have a negligible effect on the conclusions presented here.

8.) Model Scenarios

Model scenarios were used to explore different hypotheses for the late preindustrial Holocene (LPIH) increase in methane concentrations. First the latitudinal constraints the IPD imposed on methane sources were examined by calculating the source strength of a limited number of individual boxes. Next, this result was compared to a similar result obtained from a 3-box model. Then scenarios in which the strength of natural sources (N1 and N2), anthropogenic sources (A1 and A2), and both natural and anthropogenic sources (N2+A1 and N2+A2 with a 50% reduction in per-capita emissions) were varied are described. These scenarios were based on specific hypotheses for changes in the LPIH methane emissions.

Finally scenarios with a range of changes in per-capita emissions through time are considered. The model was allowed to spin up for 100 years prior to the start of each scenario to allow the sources and sinks to reach steady state.

8.1) Constraining the latitudinal changes in LPIH sources.

The global methane budget can be used to solve for two unknown parameters since the ice core records provide two constraints (concentrations in Greenland and Antarctica). The modern distribution of sources can also be used to provide additional constraints. In addition to the sink distribution and interhemispheric transport constraints discussed earlier, work on the modern distribution of sources has shown that emissions south of 30°S are ~11-15 Tg CH₄/yr and emissions north of 60°N are ~15 Tg CH₄/yr (33, 40, 41). These modern distributions include some anthropogenic sources and provide an upper boundary for LPIH sources from these latitudes.

Fig. S8 shows the methane emissions from three different Latitudinal Scenarios (L1-3) which solved the global methane budget with the ice core methane concentrations. In L1 the global methane budget was solved using the tropical NH and SH boxes (box 3 [0-30°S] vs. box 4 [0-30°N]) while all other parameters (sources, sinks, transport) were left constant. It would be surprising if the entire budget was controlled by changes in only tropical sources, so this scenario is considered an end member. In L2 the global methane budget was solved using the combined source strength from the tropical boxes (3-4 [30°S-30°N]) vs. the subtropical NH box 5 [30-60°N]. To do this a fixed ratio between the tropical boxes was used with box 3 [0-30°S] accounting for 52% of the tropical emissions and box 4 [0-30°N] accounting for 48% of the tropical emissions. Lastly, in L3 the global methane budget was solved using the combined source strength from the tropical boxes (3-4 [30°S-30°N]) vs. the combined source strength of the NH extratropical boxes (5-6 [30-90°N]). The ratio between the tropical boxes was the same as in L2 and the ratio between the NH extratropical boxes was 75% in box 5 [30-60°N] and 25% in box 6 [60-90°N]. These latitudinal scenarios encompass all the solvable realistic combinations of source emissions that could explain the observations of globally increasing methane concentrations while maintaining a roughly constant IPD. They demonstrate that the net source changes in the late Holocene involved predominantly increasing sources from the tropics and moderate increases in the extratropical NH with some centennial scale variability. To obtain the zonal change in emissions reported in Table 1 of the main paper the linear regression of the emissions from 800 B.C.E. to 1400 C.E. from L1-3 was calculated from each latitude band. The linear regression was used because the lowpass filtered results contained multidecadal scale variability and this work is focused on the multicentennial scale change. The magnitude of the change in emissions is sensitive to the assumed atmospheric lifetime of methane. This sensitivity will be discussed in greater detail in section 9.

The latitudinal scenarios did not examine scenarios where extratropical SH sources changed because they are a small proportion of the total budget (~5%) and could thus not have had a large impact on changes in LPIH source distributions. Qualitatively, however, if source changes did occur in the extratropical SH they would have to be equal in magnitude but of the opposite sign in the extratropical NH in order to obtain the same IPD and the tropical sources would also respond with the opposite sign in order to maintain the global concentration.

8.2) Comparison with a 3-box model.

It is useful to compare the model results discussed above with a previously published model. Fig. S9 shows the calculated emissions using a 3-box model (30). This model assumed a constant source strength in the SH extratropical regions (30°S-90°S) and then solved for tropical and NH extratropical sources using the global methane budget and the observed polar concentrations. The lifetimes in the boxes were changed to 13.3, 7.4, and 24.3 years for the NH, tropical, and SH boxes respectively (yielding a global average lifetime of 10.2 years) to yield parameters consistent with EBAMM. The SH source strength was set to 7.5 Tg/yr which is equivalent to the scenario L3 discussed above when the EBAMM boxes are combined to yield the same zonal regions as the 3 box model. The calculated tropical and NH extratropical emissions are essentially identical between EBAMM and the 3 box model which again shows that the LPIH increase in emissions must have come primarily from tropical regions.

8.3) Scenarios for LPIH source histories based on estimates from the literature.

There were six scenarios discussed in the main text, two having variable natural emissions and no anthropogenic emissions (N1 & N2) (42, 43), two having constant natural emissions and variable anthropogenic emissions (A1 & A2) (44, 45), and two with combined variations in natural and anthropogenic emissions (N2+A1 and N2+A2 with a 50% reduction in per-capita emissions). Since the original studies which these scenarios were based on did not all include the same set of base natural sources and in some cases recent research has indicated that previous assumptions about particular sources have been inaccurate, a consistent set of base natural sources were used here for all of the scenarios. The base natural sources included wild animals (15 Tg/yr), termites (20 Tg/yr), ocean (1 Tg/yr), geologic (30 Tg/yr), and biomass burning (17 Tg/yr). The estimate for wild animals and termite emissions came from Houweling et al., (2000). The estimate for ocean emissions came from Rhee et al., (2009). Recent estimates of geologic and biomass burning emissions vary widely so emissions that were roughly in the middle of previous estimates and which also balance the $\delta^{13}\text{CH}_4$ budget in EBAMM were used (47-51) (Fig. S11). The latitudinal distribution of the natural sources as well as the $\delta^{13}\text{C}$ values used in the model are shown in Table S1.

For each of these scenarios, first the model's tropical vs. boreal wetland source strength was adjusted so that the total source distribution produces the correct concentration and IPD values at ~1400 C.E. Then for scenarios N1-2 the anomaly of the wetland emissions from the literature estimate was used to drive the change in emissions through time. In scenarios A1-2 the change in anthropogenic emissions was driven by changes in population (described in section 8.3.3). The concentration and IPD from these model runs are shown in Fig. 2 and Table 1 of the main text and the emissions for each model run are plotted in Fig. S10. The resulting carbon isotopic composition ($\delta^{13}\text{CH}_4$) is shown for each of the scenarios in Fig. S11.

8.3.1) Scenario N1: TRENCH wetland emissions from Konijnendijk et al., (2011).

TRENCH (TRansient Emissions of Natural CH_4) is a coarse grid transient model forced by global ice volume, greenhouse gases, and insolation and was used to estimate orbital timescale variations in global wetland emissions over the past 650 ka (42). TRENCH used the climate output from the CLIMate and BiosphERe model (CLIMBER-2, (52)) which contained atmosphere, ocean, and vegetation components. These models have a resolution of 10° latitude by 51.43° longitude and the emissions from this grid spacing were combined into 30° zonal bands to match the resolution of EBAMM.

8.3.2) Scenario N2: Natural emissions from Singarayer et al., (2011).

Singarayer et al., (2011) produced model snapshots at 1 ka intervals over the past 130 ka using the coupled ocean-atmosphere Hadley Centre climate model (HadCM3) and then used the resulting climatologies as input to the Sheffield Dynamic Global Vegetation Model (SDGVM) coupled to a wetland methane emission model that predicts the location of vegetation, wetlands, methane emissions, and Volatile Organic Compound (VOC) emissions. In addition to wetlands the SDGVM has a fire module which contributes to methane emissions from biomass burning. Their models are forced by varying orbital configurations, greenhouse gases (CO₂, CH₄, and N₂O), ice sheet extent and sea level. The change in methane emissions over the LPIH predicted by this model were applied to the “wetlands” source in EBAMM. The emissions from the original model grid were combined into 30° zonal bands to match the resolution of EBAMM.

8.3.3) Scenario A1: Natural and anthropogenic emissions after Houweling et al., (2000).

Houweling et al., (2000) provided a holistic estimate of the pre-industrial methane budget in order to constrain the magnitude of wetland methane emissions. Their study focused on the average concentration between 1500-1800 C.E. and many of the individual source estimates were for the year 1500 C.E. To match the concentration and IPD data at 1400 C.E. the wetland emissions in scenario A1 were set to 96 Tg/yr. This is much lower than their estimate of 163 Tg/yr ($\pm 2\sigma$ range of 130-194 Tg/yr), however this work assumed a methane lifetime of 10 years whereas Houweling et al., (2000) used a methane lifetime of 7.2 years. In a sensitivity test where a methane lifetime of 8 years was used (discussed in section 9 below) wetland emissions were set to 135 Tg/yr, which agrees with their estimate within their uncertainty range. The latitudinal distribution of anthropogenic sources was coupled to the time dependent latitudinal distribution of population by binning global population from the HYDE 3.1 database (53) into the 30° zonal distribution of EBAMM, then interpolating those values for each time step and, finally, normalizing this to the global total population at that time step. The strength of the anthropogenic source was then multiplied by these normalized values to obtain the latitudinal distribution of each source at each time step. Since there is no evidence of pre-industrial rice emissions outside of Asia, this source was treated separately from the other anthropogenic emissions. The population from 60-140°E and 10°S-50°N (54) was binned into EBAMM boxes 3, 4 and 5 and this distribution for rice emissions was used in the same manner as for other global anthropogenic emissions. The global population and the population in the rice producing part of Asia are shown in Fig. S12. This scenario sets the following emissions in the year 1500 C.E.: rice agriculture = 10 Tg/yr, domestic ruminants = 5 Tg/yr, and landfills = 5 Tg/yr and assumes the per-capita emissions of rice were constant throughout the LPIH.

The impact of using a per-capita scaling for anthropogenic biomass burning emissions was also examined (Fig. S13). Scaling anthropogenic biomass burning to population causes the ¹³CH₄ to increase through time which is inconsistent with ice core $\delta^{13}\text{CH}_4$ data from Greenland (NEEM (47)) and Antarctica (WDC05A (51); Law Dome (50)). As noted previously (47), the long term late Holocene change in $\delta^{13}\text{CH}_4$ is consistent with a predominantly biogenic increase in sources. By leaving all (natural and anthropogenic) biomass burning emissions constant, the millennial scale $\delta^{13}\text{CH}_4$ trend, which in the model is caused by increasing biogenic emissions from wetlands and rice agriculture, is able to match the observations (Fig. S11). It is possible to force the model to fit short term variations in the $\delta^{13}\text{CH}_4$ record by adjusting biomass burning emissions (as has been done previously (47, 50)), however the centennial scale variations in this source obscure the long term changes in emissions that are the focus of this work. Linearly

scaling biomass burning emissions to charcoal records presents challenges because of an incomplete understanding of how charcoal accumulation rates relates to burned area, fire intensity, and severity across a range of environments and vegetation types (55) and is beyond the scope of the present work.

8.3.4) Scenario A2: Natural and anthropogenic emissions after Ruddiman (2007).

The early anthropogenic hypothesis provided an upper level estimate of anthropogenic emissions in the LPIH. This scenario was based on estimates of emissions from Table 5 in Ruddiman (2007) and the rice agriculture upper limit of 32 Tg/yr in 1500 C.E was used. This scenario also assumes that per-capita emissions of rice were constant throughout the LPIH. The other anthropogenic emissions were domestic ruminants = 7 Tg/yr, and landfills = 4 Tg/yr. As in previous scenarios, tropical and boreal wetland emissions were used to adjust the concentration and IPD to match the data at 1400 C.E.

The full early anthropogenic hypothesis includes decreasing natural sources and uses increasing anthropogenic sources to balance the budget. However, this decrease in natural emissions was not predicted by either of the models incorporating only natural emissions. Also, if natural emissions were decreasing, there would need to be an even larger increase in anthropogenic emissions over the LPIH which would cause the IPD to increase over time and is not supported by the data. Theoretically if the decrease in natural emissions came primarily from boreal latitudes it could contribute to balancing the IPD, but this would represent a dramatic decrease in boreal emissions which was not suggested in either of the models of natural emissions. This scenario kept natural sources constant to isolate the effect that increasing anthropogenic emissions would have on methane concentrations and the IPD.

Note that since scenarios A1 & A2 have constant natural emissions their model results would be approximately equivalent to what would be expected from N1+A1 and N1+A2 since scenario N1 contains only small changes in natural emissions.

8.3.5) Combined scenario N2+A1.

This scenario contains the anthropogenic emission changes from A1 combined with the natural emission changes from N2. It assumes that per-capita changes in emissions stay constant through the LPIH (Fig. S14).

8.3.6) Combined scenario N2+A2 with a 50% reduction in per-capita emissions from rice agriculture.

This scenario contains the anthropogenic emission changes from A2 combined with the natural emission changes from N2 with the addition that per-capita emissions of methane from rice agriculture decrease by 50% between 1000 B.C.E. and 1500 C.E. (Fig. S14). Other anthropogenic emissions (landfills and domestic ruminants) were assumed to have a constant per-capita relationship through time.

8.3.7) Alternative changes in per-capita emissions from rice agriculture.

The early anthropogenic hypothesis states that LPIH methane emissions from rice must have been disproportionately large because early farming methods were not as efficient as they are today and therefore per-capita emissions of methane from rice agriculture would have been larger in the LPIH than during modern times (56-58). This is consistent with theoretical work indicating that land use intensifies as population increases ((59), and a review in (58)). While

there is a paucity of data on per-capita changes in land use (e.g. (60)), simple assumptions have been proposed and can be tested within the modeling framework used here.

Two recent studies have estimated per-capita land use changes over the Holocene (58, 61) and while they disagree on the absolute magnitude of land use per-capita over the LPIH, both of them predict a 75% to 80% decrease in the relative per-capita land use between approximately 1000 B.C.E. and 1500 C.E. Since a quantitative relationship between land use and methane emissions from rice agriculture does not exist, the per-capita emissions used here were based on population and the literature estimate of anthropogenic rice agriculture emissions in the year 1500 C.E., and then the change in per-capita emissions was scaled to the change in land use in a relative sense. Three levels of changing per-capita emissions were tested, first, per-capita emissions remained constant through time, second, per-capita emissions decreased by 50% between 1000 B.C.E. and 1500 C.E., and third, per-capita emissions decreased by 75% between 1000 B.C.E. and 1500 C.E. (Fig. S14). These three levels of per-capita emission changes were used with the combined N2+A1 and N2+A2 scenarios as a sensitivity test to see which level of per-capita scaling provided the best fit to the concentration data (Fig. S15). The primary impact of changing per-capita emissions through time was to increase the early anthropogenic emissions (i.e. emissions at 800 B.C.E.) which had the effect of reducing the change in emissions between 800 B.C.E. and 1400 C.E. For the scenarios that used the anthropogenic emissions from A1, the best fit to the data was achieved with constant per-capita emissions from rice agriculture. For the scenarios that used anthropogenic emissions from A2, the best fit to the data was achieved with a 50% reduction in per-capita emissions from rice agriculture. Both scenarios which used a 75% reduction in per-capita emissions provided a poor fit to the concentration data (Fig. S15).

9) **Sensitivity to changes in the assumed lifetime of methane.**

Very recently the preindustrial lifetime of methane was assessed as part of the Atmospheric Chemistry and Climate Model Intercomparison Project (ACCMIP) (35). This work examined the change in the lifetime of methane between preindustrial and modern times using 17 state of the art global atmospheric chemistry models and found that the multi-model mean and standard deviation of the preindustrial lifetime of methane was 10.1 ± 1.7 years.

In its simplest form, the global methane budget can be expressed as $dB/dt = S - B/\tau$ where B is the total atmospheric burden of methane (Tg), S is the total source strength (Tg yr⁻¹), and τ is the lifetime of methane (yr). The atmospheric burden is a function of the concentration and the total mass of the atmosphere. At steady state ($dB/dt = 0$), the equation can be rearranged as $S = B/\tau$, implying that within a box modeling framework the strength of the sources has an inverse relationship with the lifetime of methane.

To examine how different lifetimes affected the results presented here the scenarios were re-run with lifetimes of 8 and 12 years (Fig. S16, S17, and Table S2). The primary impact on the results of changing the lifetime from 10 years to 8 years (12 years) is that it increased (decreased) the magnitude of emissions needed to support a given atmospheric concentration as well as the magnitude of the change in emissions over the LPIH (Table S2). So, with a lifetime of 8 years (12 years), the change in emissions between 800 B.C.E. and 1400 C.E. calculated from scenarios L1-3 is ~29 Tg/yr (~20 Tg/yr). Regardless of this range, however, the trend in the emission changes was identical regardless of which lifetime was chosen. The model scenarios were each tuned using the tropical vs. boreal wetland source strength so that the distribution and strength of emissions produced the correct concentration and IPD values at ~1400 C.E. The magnitude of biomass burning was also adjusted since the consumption of methane by OH

causes an isotopic fractionation. For a lifetime of 8 years (12 years) biomass burning was set to 25 Tg/yr (12 Tg/yr). Doing this produced essentially identical $\delta^{13}\text{CH}_4$ model output as in Fig. S11. Then the same magnitude of change in emissions over the LPIH as was used in the main paper (i.e. the changes in emissions from Table 1) was used to drive these scenarios through time (Fig. S17). While the different assumed lifetimes have an impact on the change in concentrations, the IPD was relatively insensitive to the choice of a lifetime. Depending on the assumed lifetime, the combined scenarios would need to be changed in order for them to match the concentrations. With a lifetime of 10 years, the emissions in the “N2+A2 with -50% per-capita” scenario change by 24 Tg/yr (Table 1). Therefore, if the lifetime of methane were set to 8 years (12 years), the change in emissions would need to be increased by 5 Tg/yr to 29 Tg/yr (decreased by 4 Tg/yr to 20 Tg/yr) as indicated by scenarios L1-3 run with different assumed lifetimes (Table S2). This change in emissions would need to occur in the tropical wetlands source since this source has a negligible impact on the IPG. Changing the scenario in this way to account for different assumed lifetimes would not affect the primary conclusion that changes in emissions from both natural and anthropogenic sources were needed to fit the concentration data from both poles.

References and Notes:

1. L. E. Mitchell, E. J. Brook, T. Sowers, J. R. McConnell, K. Taylor, Multidecadal variability of atmospheric methane, 1000-1800 CE. *J. Geophys. Res.-Biogeosci.* **116**, (Apr, 2011).
2. A. M. Grachev, E. J. Brook, J. P. Severinghaus, N. G. Piasias, Relative timing and variability of atmospheric methane and GISP2 oxygen isotopes between 68 and 86 ka. *Glob. Biogeochem. Cycle* **23**, 10 (Apr, 2009).
3. A. M. Grachev, E. J. Brook, J. P. Severinghaus, Abrupt changes in atmospheric methane at the MIS 5b-5a transition. *Geophys. Res. Lett.* **34**, 5 (Oct, 2007).
4. E. J. Dlugokencky *et al.*, Conversion of NOAA atmospheric dry air CH₄ mole fractions to a gravimetrically prepared standard scale. *J. Geophys. Res.-Atmos.* **110**, 8 (Sep, 2005).
5. H. Craig, Y. Horibe, T. Sowers, Gravitational Separation of Gases and Isotopes in Polar Ice Caps. *Science* **242**, 1675 (Dec, 1988).
6. J. Schwander, in *The Environmental Record in Glaciers and Ice Sheets*, H. Oeschger, C. C. Langway, Eds. (John Wiley, Chichester [England] ; New York :, 1989), pp. 53-67.
7. T. Sowers, M. Bender, D. Raynaud, Elemental and Isotopic Composition of Occluded O₂ and N₂ in Polar Ice. *J. Geophys. Res.-Atmos.* **94**, 5137 (Apr, 1989).
8. T. Sowers, M. Bender, D. Raynaud, Y. S. Korotkevich, d¹⁵N of N₂ in Air Trapped in Polar Ice: a Tracer of Gas Transport in the Fim and a Possible Constraint on Ice Age-Gas Age Differences. *J. Geophys. Res.-Atmos.* **97**, 15683 (Oct, 1992).
9. T. Kobashi *et al.*, Persistent multi-decadal Greenland temperature fluctuation through the last millennium. *Clim. Change* **100**, 733 (Jun, 2010).
10. R. A. Rohde, P. B. Price, R. C. Bay, N. E. Bramall, In situ microbial metabolism as a cause of gas anomalies in ice. *Proc. Natl. Acad. Sci. U. S. A.* **105**, 8667 (Jun, 2008).
11. A. Schilt *et al.*, Atmospheric nitrous oxide during the last 140,000 years. *Earth and Planetary Science Letters* **300**, 33 (Nov, 2010).
12. C. de Boor, *A Practical Guide to Splines*. (Springer, New York, 2001).
13. P. A. Mayewski *et al.*, Major features and forcing of high-latitude northern hemisphere atmospheric circulation using a 110,000-year-long glaciochemical series. *J. Geophys. Res.-Oceans* **102**, 26345 (Nov, 1997).
14. R. H. Rhodes *et al.*, Continuous methane measurements from a late Holocene Greenland ice core: Atmospheric and in-situ signals. *Earth and Planetary Science Letters* **368**, 9 (4/15/, 2013).
15. R. B. Alley *et al.*, Visual-stratigraphic dating of the GISP2 ice core: Basis, reproducibility, and application. *J. Geophys. Res.-Oceans* **102**, 26367 (Nov, 1997).
16. K. M. Cuffey, G. D. Clow, Temperature, accumulation, and ice sheet elevation in central Greenland through the last deglacial transition. *J. Geophys. Res.-Oceans* **102**, 26383 (Nov, 1997).
17. T. Kobashi *et al.*, High variability of Greenland surface temperature over the past 4000 years estimated from trapped air in an ice core. *Geophys. Res. Lett.* **38**, (Nov, 2011).
18. J. M. Fegyveresi *et al.*, Late-Holocene climate evolution at the WAIS Divide site, West Antarctica: bubble number-density estimates. *J. of Glaciol.* **57**, 629 (2011).
19. A. J. Orsi, B. D. Cornuelle, J. P. Severinghaus, Little Ice Age cold interval in West Antarctica: Evidence from borehole temperature at the West Antarctic Ice Sheet (WAIS) Divide. *Geophys. Res. Lett.* **39**, L09710 (2012).
20. M. O. Battle *et al.*, Controls on the movement and composition of firn air at the West Antarctic Ice Sheet Divide. *Atmos. Chem. Phys.* **11**, 11007 (2011).
21. C. Buizert *et al.*, Gas transport in firn: multiple-tracer characterisation and model intercomparison for NEEM, Northern Greenland. *Atmos. Chem. Phys.* **12**, 4259 (2012).
22. E. Witrant *et al.*, A new multi-gas constrained model of trace gas non-homogeneous transport in firn: evaluation and behaviour at eleven polar sites. *Atmos. Chem. Phys.* **12**, 11465 (2012).

23. C. Buizert, T. Sowers, T. Blunier, Assessment of diffusive isotopic fractionation in polar firn, and application to ice core trace gas records. *Earth and Planetary Science Letters* **361**, 110 (1/1/, 2013).
24. M. M. Herron, C. C. Langway, Firn Densification: An Empirical Model. *J. of Glaciol.* **25**, 373 (1980).
25. K. M. Cuffey, W. Paterson, *The physics of glaciers*. (Academic Press, 2010).
26. D. A. Meese *et al.*, The Accumulation Record from the GISP2 Core as an Indicator of Climate Change Throughout the Holocene. *Science* **266**, 1680 (Dec, 1994).
27. D. M. Etheridge, L. P. Steele, R. J. Francey, R. L. Langenfelds, Atmospheric methane between 1000 AD and present: Evidence of anthropogenic emissions and climatic variability. *J. Geophys. Res.-Atmos.* **103**, 15979 (Jul, 1998).
28. C. MacFarling Meure *et al.*, Law Dome CO₂, CH₄ and N₂O ice core records extended to 2000 years BP. *Geophys. Res. Let.* **33**, 4 (Jul, 2006).
29. E. J. Dlugokencky *et al.*, A dramatic decrease in the growth rate of atmospheric methane in the northern hemisphere during 1992. *Geophys. Res. Let.* **21**, 45 (Jan, 1994).
30. J. Chappellaz *et al.*, Changes in the atmospheric CH₄ gradient between Greenland and Antarctica during the Holocene. *J. Geophys. Res.-Atmos.* **102**, 15987 (Jul, 1997).
31. T. Nakazawa *et al.*, Differences of the Atmospheric CH₄ Concentration Between the Arctic and Antarctic Regions in Pre-Industrial/Pre-Agricultural Era. *Geophys. Res. Let.* **20**, 943 (May, 1993).
32. T. Marik, Ph.D., University of Heidelberg (1998).
33. R. Hein, P. J. Crutzen, M. Heimann, An inverse modeling approach to investigate the global atmospheric methane cycle. *Glob. Biogeochem. Cycle* **11**, 43 (Mar, 1997).
34. P. O. Hopcroft, P. J. Valdes, D. J. Beerling, Simulating idealized Dansgaard-Oeschger events and their potential impacts on the global methane cycle. *Quat. Sci. Rev.* **30**, 3258 (Nov, 2011).
35. V. Naik *et al.*, Preindustrial to present-day changes in tropospheric hydroxyl radical and methane lifetime from the Atmospheric Chemistry and Climate Model Intercomparison Project (ACCMIP). *Atmos. Chem. Phys.* **13**, 5277 (2013).
36. S. L. Harder, D. T. Shindell, G. A. Schmidt, E. J. Brook, A global climate model study of CH₄ emissions during the Holocene and glacial-interglacial transitions constrained by ice core data. *Glob. Biogeochem. Cycle* **21**, 13 (Feb, 2007).
37. J. O. Kaplan, G. Folberth, D. A. Hauglustaine, Role of methane and biogenic volatile organic compound sources in late glacial and Holocene fluctuations of atmospheric methane concentrations. *Glob. Biogeochem. Cycle* **20**, 16 (Jun, 2006).
38. C. M. Trudinger *et al.*, Modeling air movement and bubble trapping in firn. *J. Geophys. Res.-Atmos.* **102**, 6747 (Mar, 1997).
39. C. Buizert *et al.*, Gas transport in firn: multiple-tracer characterisation and model intercomparison for NEEM, Northern Greenland. *Atmos. Chem. Phys. Discuss.* **11**, 15975 (2011).
40. I. Fung *et al.*, 3-Dimensional Model Synthesis of the Global Methane Cycle. *J. Geophys. Res.-Atmos.* **96**, 13033 (Jul, 1991).
41. P. Bergamaschi *et al.*, Inverse modeling of global and regional CH₄ emissions using SCIAMACHY satellite retrievals. *J. Geophys. Res.-Atmos.* **114**, (Nov, 2009).
42. T. Y. M. Konijnendijk, S. L. Weber, E. Tuenter, M. van Weele, Methane variations on orbital timescales: a transient modeling experiment. *Clim. Past.* **7**, 635 (2011).
43. J. S. Singarayer, P. J. Valdes, P. Friedlingstein, S. Nelson, D. J. Beerling, Late Holocene methane rise caused by orbitally controlled increase in tropical sources. *Nature* **470**, 82 (Feb, 2011).
44. S. Houweling, F. Dentener, J. Lelieveld, Simulation of preindustrial atmospheric methane to constrain the global source strength of natural wetlands. *J. Geophys. Res.-Atmos.* **105**, 17243 (Jul, 2000).
45. W. F. Ruddiman, The early anthropogenic hypothesis: Challenges and responses. *Reviews of Geophysics* **45**, 37 (Oct, 2007).

46. T. S. Rhee, A. J. Kettle, M. O. Andreae, Methane and nitrous oxide emissions from the ocean: A reassessment using basin-wide observations in the Atlantic. *J. Geophys. Res.-Atmos.* **114**, (Jun, 2009).
47. C. J. Sapart *et al.*, Natural and anthropogenic variations in methane sources during the past two millennia. *Nature* **490**, 85 (2012).
48. G. Etiope, K. R. Lassey, R. W. Klusman, E. Boschi, Reappraisal of the fossil methane budget and related emission from geologic sources. *Geophys. Res. Lett.* **35**, (May, 2008).
49. G. Etiope, A. V. Milkov, E. Derbyshire, Did geologic emissions of methane play any role in Quaternary climate change? *Glob. Planet. Change* **61**, 79 (Mar, 2008).
50. D. F. Ferretti *et al.*, Unexpected Changes to the Global Methane Budget over the Past 2000 Years. *Science* **309**, 1714 (September 9, 2005, 2005).
51. J. A. Mischler *et al.*, Carbon and hydrogen isotopic composition of methane over the last 1000 years. *Glob. Biogeochem. Cycle* **23**, (Nov, 2009).
52. V. Petoukhov *et al.*, CLIMBER-2: a climate system model of intermediate complexity. Part I: model description and performance for present climate. *Clim. Dyn.* **16**, 1 (Jan, 2000).
53. K. K. Goldewijk, A. Beusen, P. Janssen, Long-term dynamic modeling of global population and built-up area in a spatially explicit way: HYDE 3.1. *Holocene* **20**, 565 (Jun, 2010).
54. D. Q. Fuller *et al.*, The contribution of rice agriculture and livestock pastoralism to prehistoric methane levels: An archaeological assessment. *Holocene* **21**, 743 (Aug, 2011).
55. J. R. Marlon *et al.*, Global biomass burning: a synthesis and review of Holocene paleofire records and their controls. *Quat. Sci. Rev.* **65**, 5 (Apr, 2013).
56. W. F. Ruddiman, The anthropogenic greenhouse era began thousands of years ago. *Clim. Change* **61**, 261 (Dec, 2003).
57. W. F. Ruddiman, J. S. Thomson, The case for human causes of increased atmospheric CH₄ over the last 5000 years. *Quat. Sci. Rev.* **20**, 1769 (2001).
58. W. F. Ruddiman, E. C. Ellis, Effect of per-capita land use changes on Holocene forest clearance and CO₂ emissions. *Quat. Sci. Rev.* **28**, 3011 (Dec, 2009).
59. E. Boserup, *The conditions of agricultural growth: the economics of agrarian change under population pressure.* (Transaction Books, 1965).
60. E. C. Ellis, S. M. Wang, Sustainable traditional agriculture in the Tai Lake Region of China. *Agriculture Ecosystems & Environment* **61**, 177 (Feb, 1997).
61. J. O. Kaplan *et al.*, Holocene carbon emissions as a result of anthropogenic land cover change. *Holocene* **21**, 775 (Aug, 2011).
62. E. J. Dlugokencky, P. M. Lang, A. M. Crotwell, K. A. Masaire, Atmospheric Methane Dry Air Mole Fractions from the NOAA ESRL Carbon Cycle Cooperative Global Air Sampling Network, 1983-2011, Version: 2012-09-24, Path: <ftp://ftp.cmdl.noaa.gov/ccg/ch4/flask/event/>. (2012).
63. WAIS Divide Project Members, Onset of deglacial warming in West Antarctica driven by local orbital forcing. *Nature* **500**, 440 (08/22/print, 2013).
64. Q. Zhuang *et al.*, Methane fluxes between terrestrial ecosystems and the atmosphere at northern high latitudes during the past century: A retrospective analysis with a process-based biogeochemistry model. *Glob. Biogeochem. Cycle* **18**, (Aug, 2004).
65. T. S. Bates, K. C. Kelly, J. E. Johnson, R. H. Gammon, A reevaluation of the open ocean source of methane to the atmosphere. *J. Geophys. Res.-Atmos.* **101**, 6953 (Mar, 1996).
66. M. Whiticar, H. Schaefer, Constraining past global tropospheric methane budgets with carbon and hydrogen isotope ratios in ice. *Philos. Trans. R. Soc. A-Math. Phys. Eng. Sci.* **365**, 1793 (Jul, 2007).

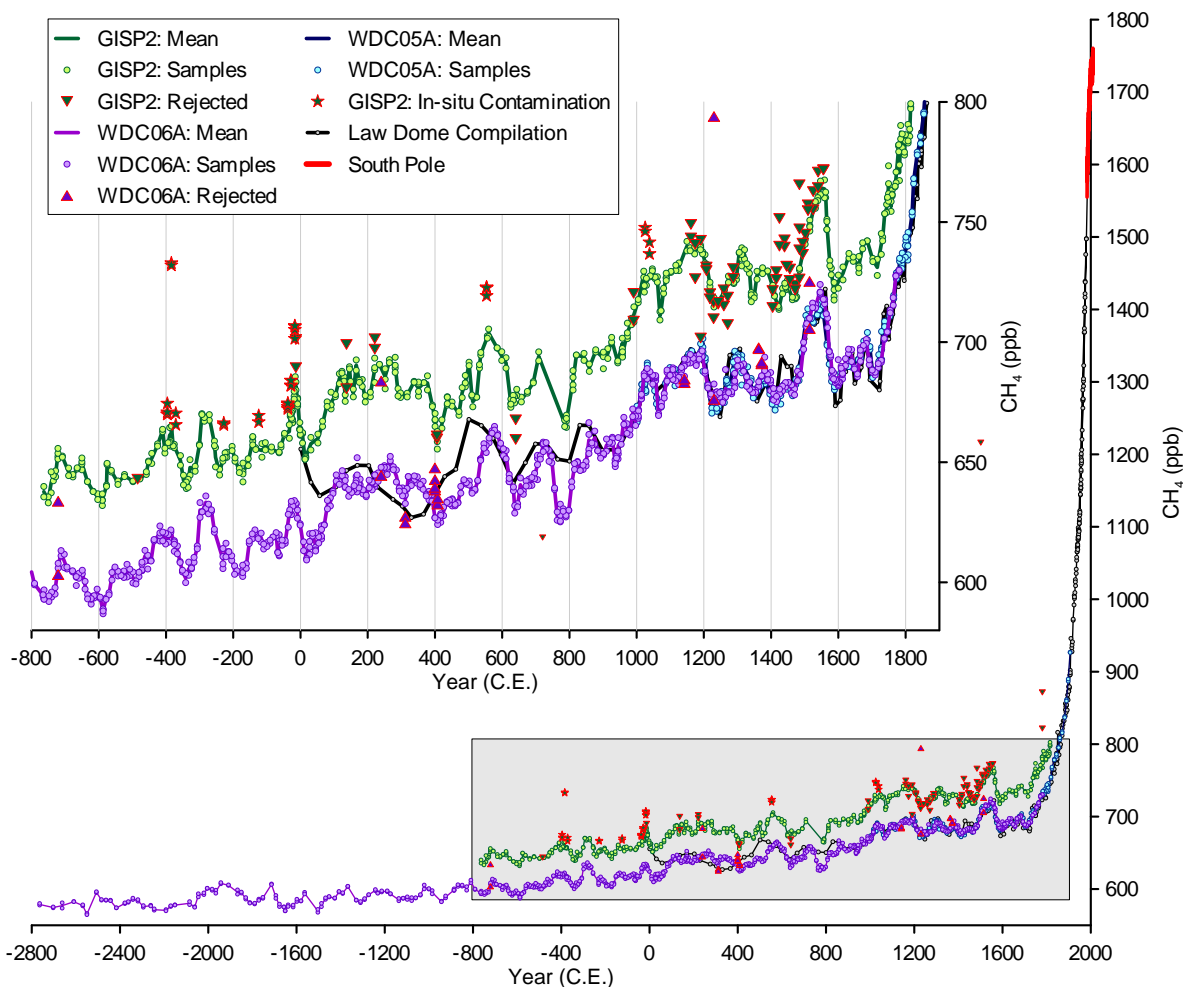


Fig. S1. Methane measurements from GISP2 (green), WAIS Divide (the main borehole WDC06A [purple] and the shallow borehole WDC05A [blue] (1)), Law Dome (black) (27, 28), and South Pole (red) (62). Circles represent individual samples and the line is linearly interpolated through the mean concentration from each depth/age. The WAIS Divide records are on a gas-age chronology derived from the WDC06A-7 layer counted ice-age chronology (63) and a dynamic firn densification model. The GISP2 timescale has been optimized to match the WAIS Divide timescale using an iterative Monte Carlo correlation technique. Also shown are rejected samples (WAIS: upwards pointing triangles, GISP: downwards pointing triangles) and GISP2 samples which were suspect of containing in-situ contamination (stars). All methane measurements are plotted on the NOAA04 calibration scale (4). Shaded box indicates the time period for this study.

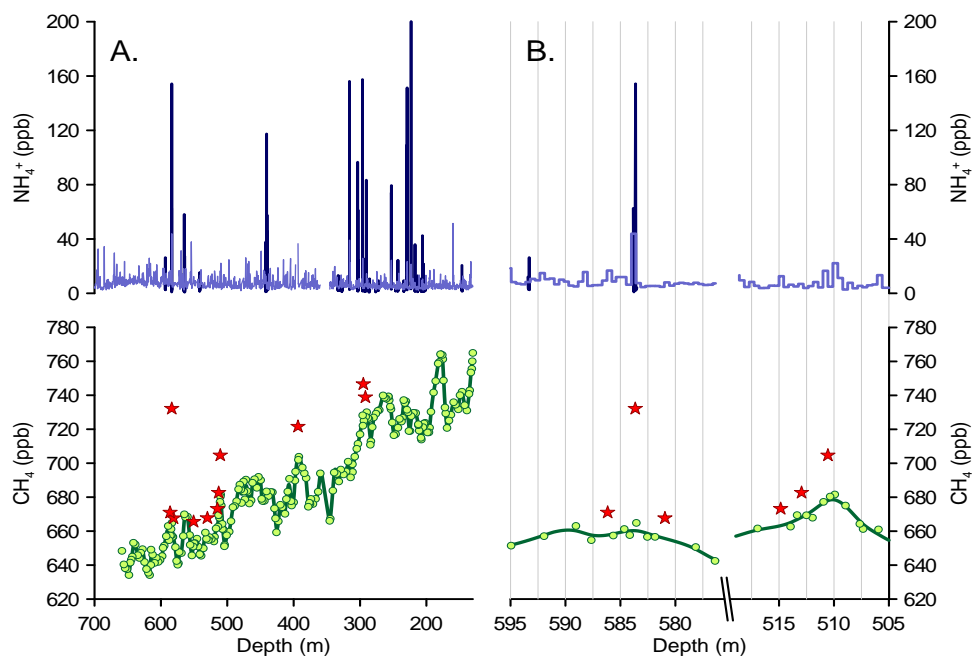


Fig. S2. GISP2 CH_4 and NH_4^+ (*13*) records in the late pre-industrial Holocene (A.), and detailed views of samples at ~510 and ~585m (B.). The line between the data points in (B.) is a spline fit to the data as discussed in the text.

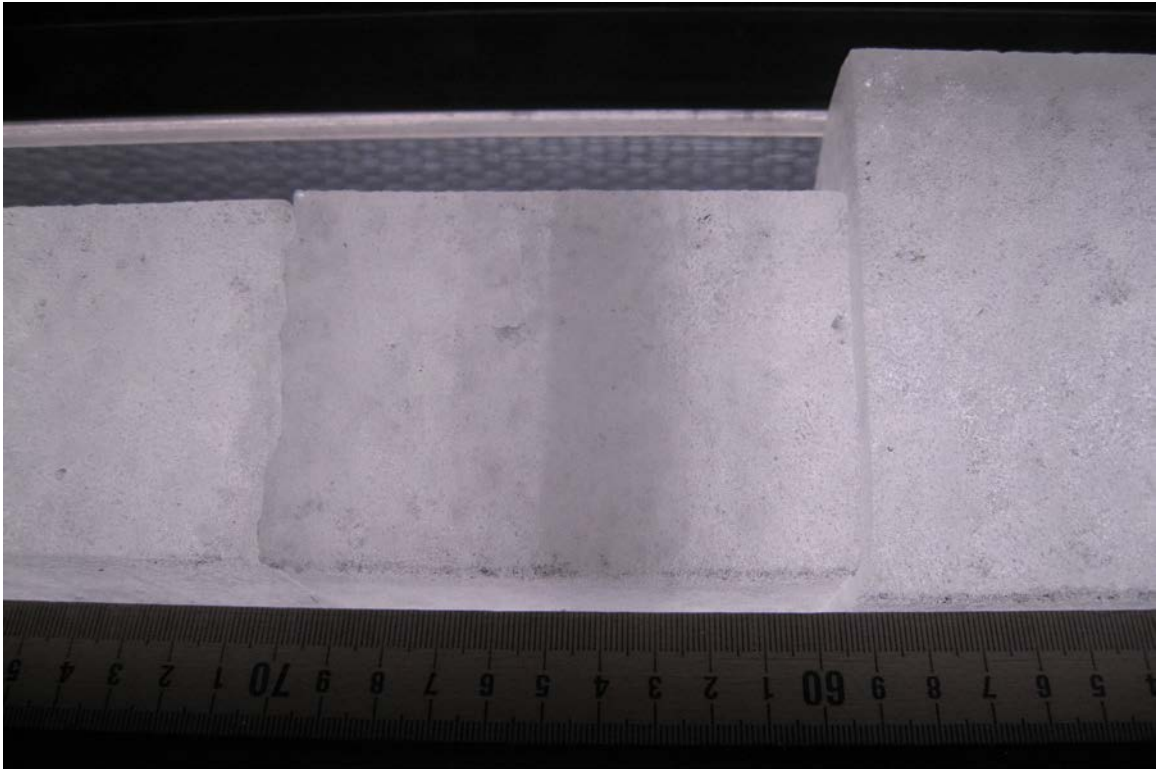


Fig. S3. Cloudy band in the GISP2 methane sample which had methane concentrations ~ 70 ppb higher than nearby samples. The sample depths are 583.6-583.7 m and the cloudy band associated with the NH_4^+ spike is visible from 583.63-583.65 m. Photo credit L. E. Mitchell.

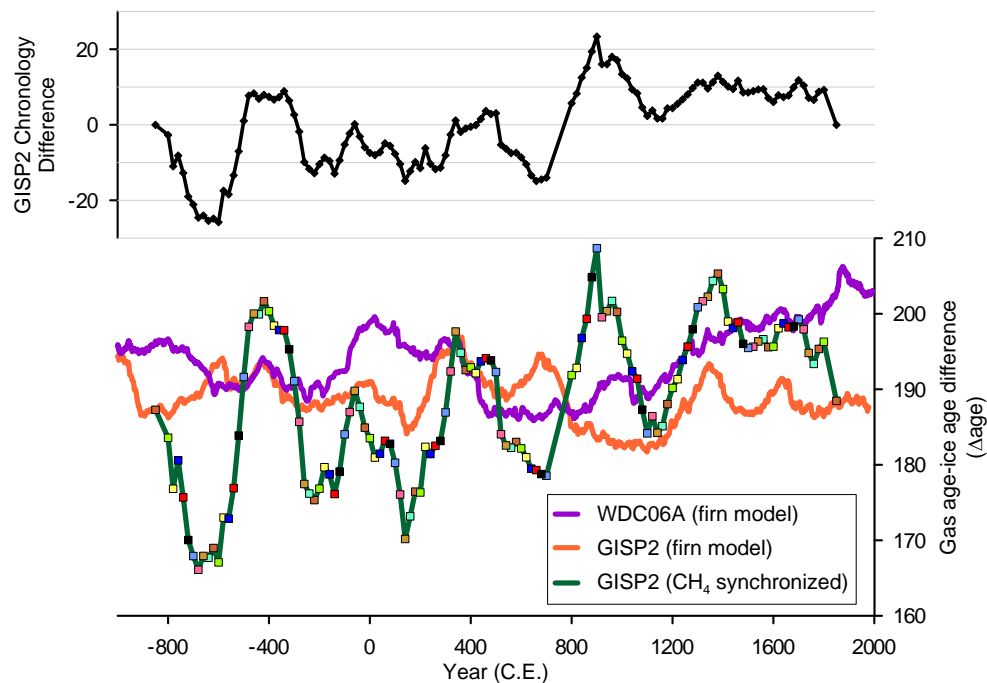


Fig. S4. The difference between the GISP2 (firm model) and GISP2 (CH₄ synchronized) chronologies (top) and Gas age-ice age difference (Δ age) for the GISP2 and WAIS Divide ice cores (bottom). Gas age chronologies for “GISP2 (firm model)” (orange) and “WDC06A (firm model)” (purple) are determined with a dynamic firm air model. The “GISP2 (CH₄ synchronized)” (green with symbols) chronology has 10 different symbol colors corresponding to the tie points of the 10 different iterative Monte Carlo chronologies which each have a spacing of 200 years. The combined chronology thus has tie points which are spaced 20 years apart.

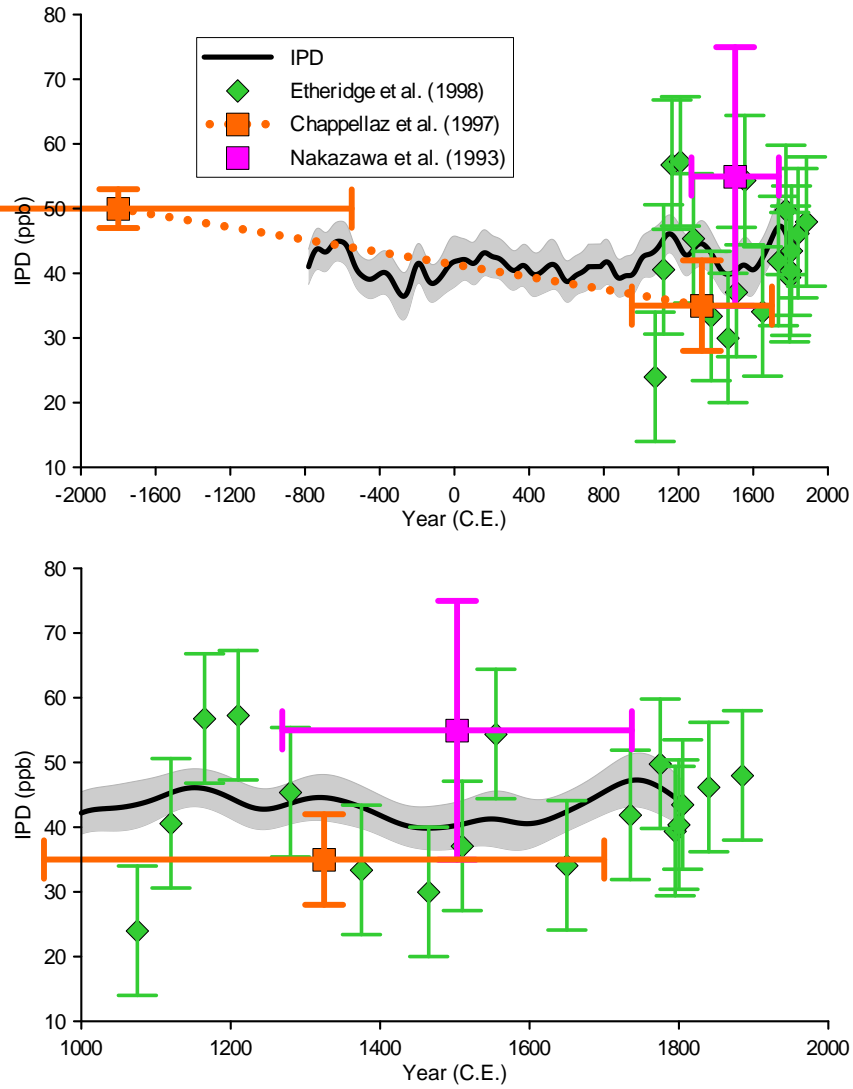


Fig. S5. Comparison with previously published estimates of the IPD (27, 30, 31) over the past 4 ka (upper) and 1 ka (lower). The IPD record presented here has been smoothed with a 20-year lowpass filter and the shaded 2σ error is determined with a Monte Carlo procedure.

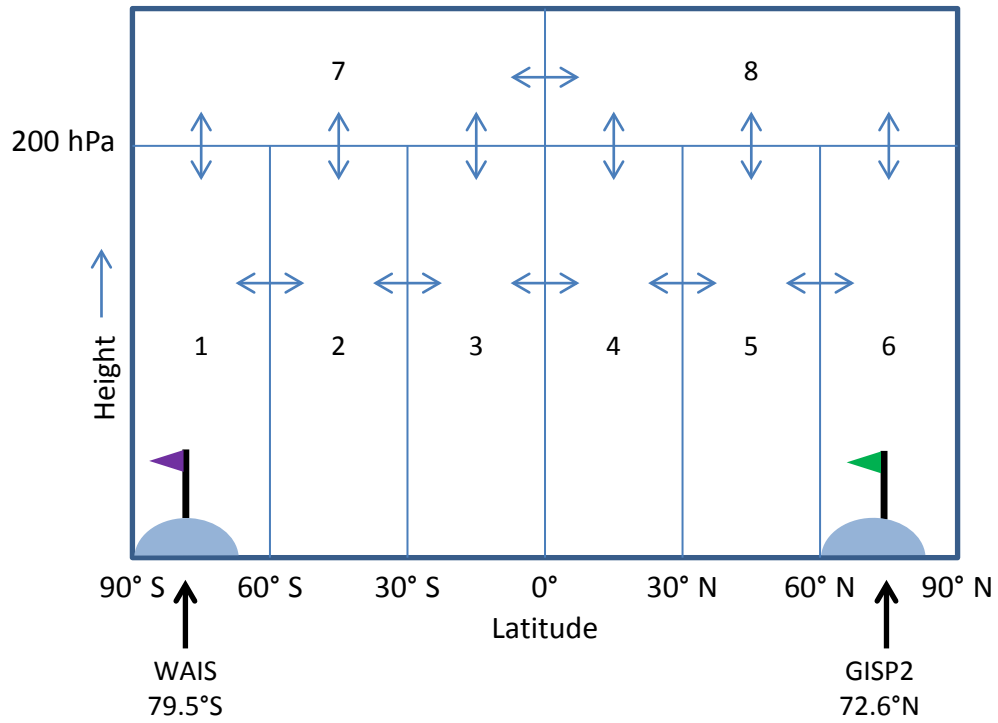


Fig. S6. Schematic diagram of the EBAMM model space. There are 6 tropospheric boxes and two stratospheric boxes separated by the tropopause at 200 hPa. Box 1 and Box 6 represent the concentrations of WAIS Divide and GISP2, respectively.

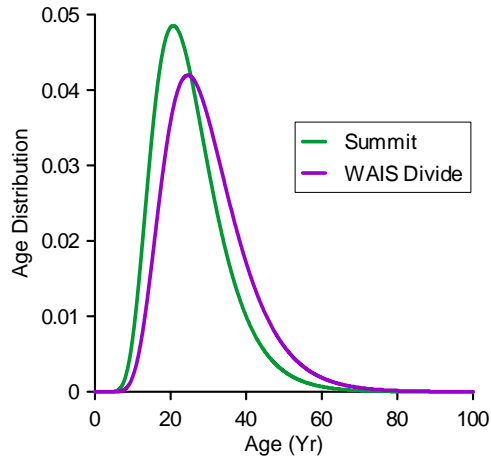


Fig. S7. Age distribution of air in the open porosity for Summit Greenland and WAIS Divide. Summit, Greenland is used instead of GISP2 because of the availability of many trace gases being measured in the Summit firn air. The Summit ice core is ~28 km away from GISP2 and should therefore have very similar smoothing characteristics.

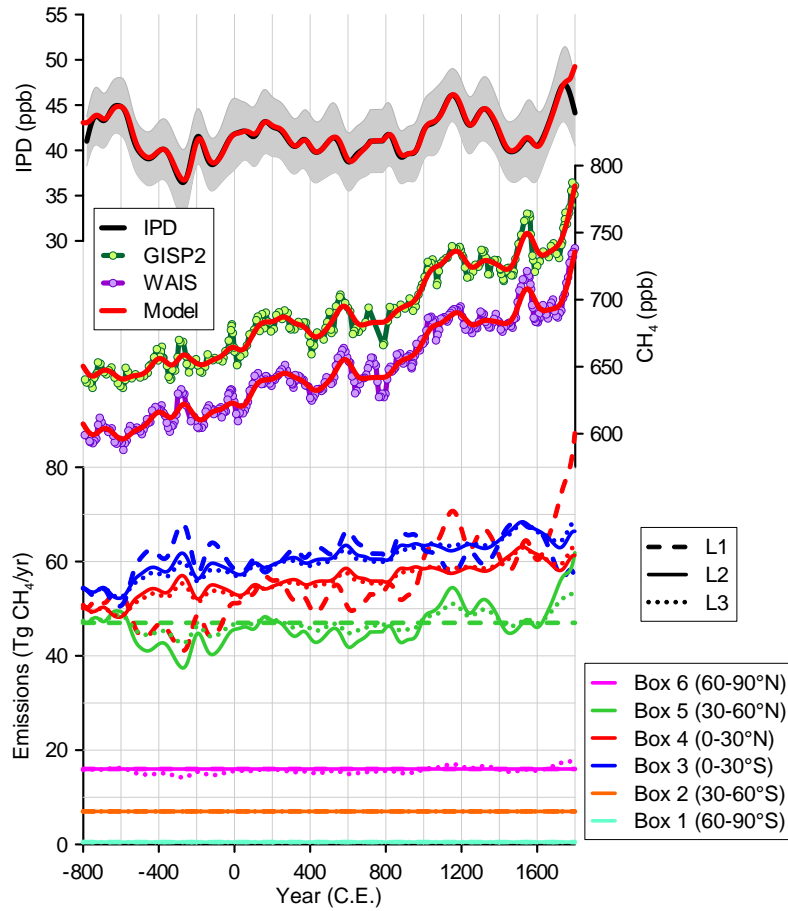


Fig. S8. EBAMM latitudinal scenarios 1-3 (L1-3). Each of the 3 scenarios obtains the same concentration and IPD results. The colors correspond to EBAMM boxes while the pattern of the line indicates scenarios L1-3. These scenarios all assume a methane lifetime of 10 years.

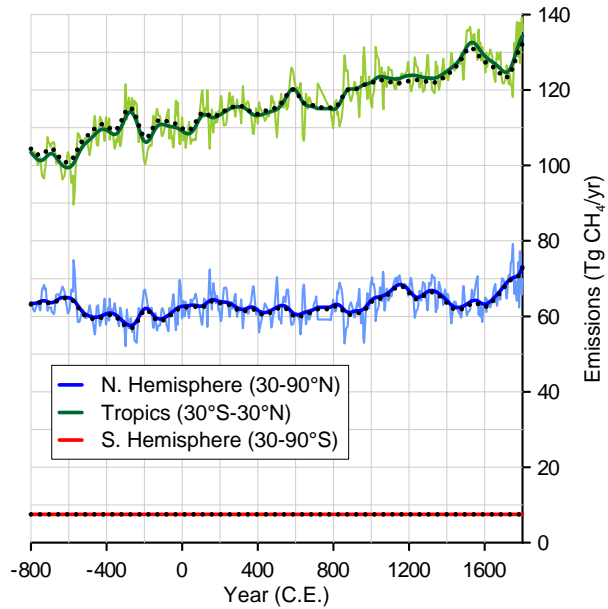


Fig. S9. 3 box model results. The 3 box model is described in (30). The light solid lines are the model results solved for the annually interpolated data, the dark solid lines are the model results solved for the 20-year lowpass filtered concentration data, and the dotted lines are the results of the EBAMM scenario L3 where the boxes have been combined to yield the same zonal regions as the 3 box model. There is a slight divergence in the tropical emissions over time as a result of a difference in the sink parameterization in EBAMM described in section 7.

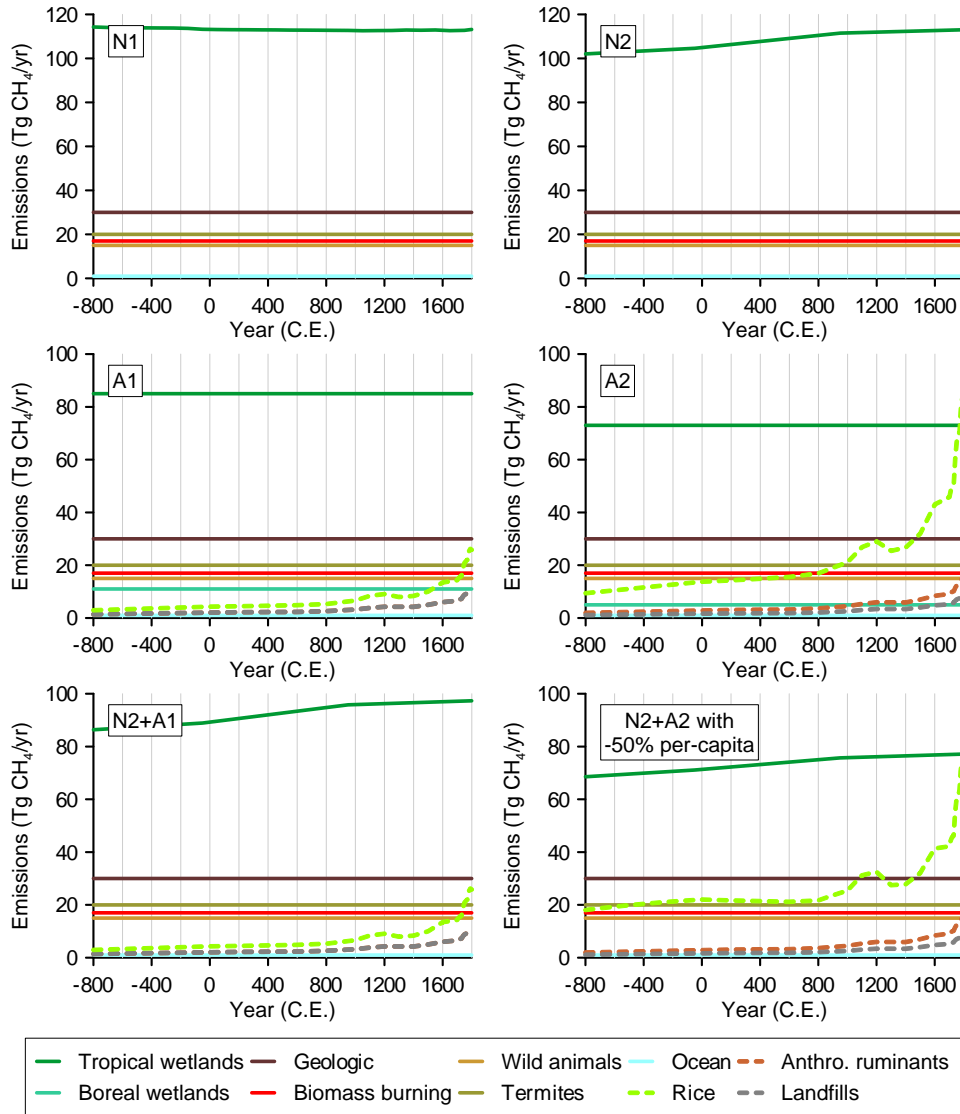


Fig. S10. Emissions for scenarios from Fig. 2 of the main text. Latitudinal distributions of natural sources are specified in Table S1 and are described for anthropogenic emissions under the description for Scenario A1. In scenarios N1-2 and the combined scenarios, all of the wetland emissions are combined into one “wetlands” source with the latitudinal distribution coming from the cited literature estimates and the tuning procedure described in section 8.3. Scenarios A1-2 have a “Tropical wetland” and “Boreal wetland” source with latitudinal distributions shown in Table S1.

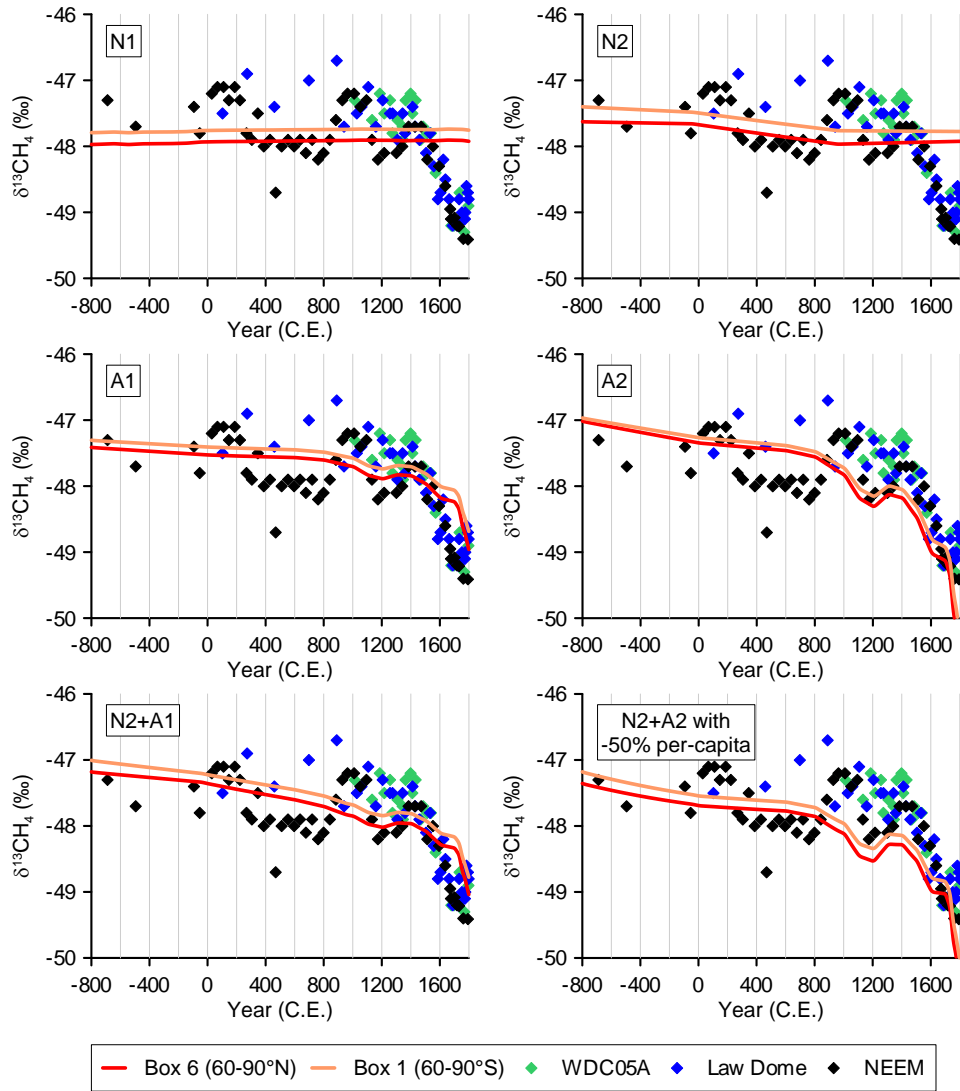


Fig. S11. Modeled $\delta^{13}\text{CH}_4$ for each of the scenarios. $\delta^{13}\text{CH}_4$ data comes from WDC05A, Antarctica (51), Law Dome, Antarctica (50), and NEEM, Greenland (47).

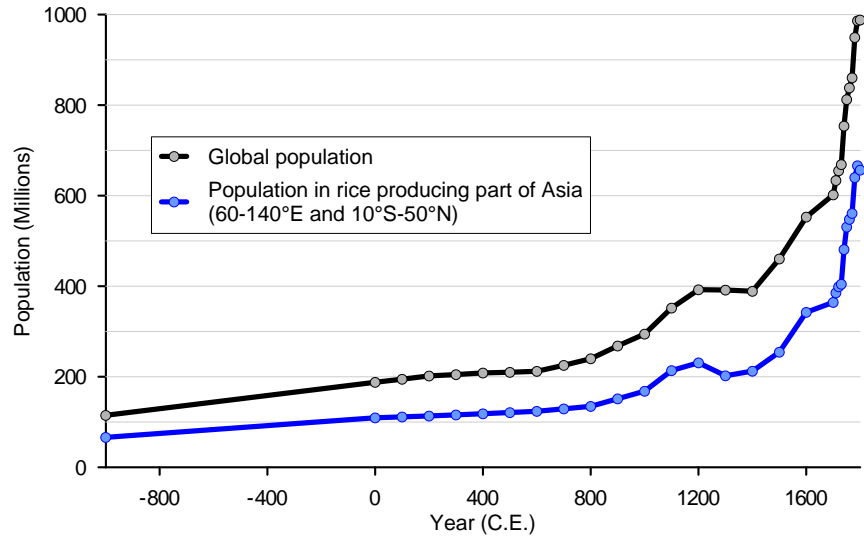


Fig S12. Population estimates used in this work derived from the HYDE 3.1 database (53). The global population was used to scale the domestic ruminant and landfill methane sources. The population in the rice producing part of Asia (between 60-140°E and 10°S-50°N) was used to scale the rice agriculture methane source. Shown here is the total population used to scale these methane sources, however the model subdivides these totals into the population in each of the latitudinal bands.

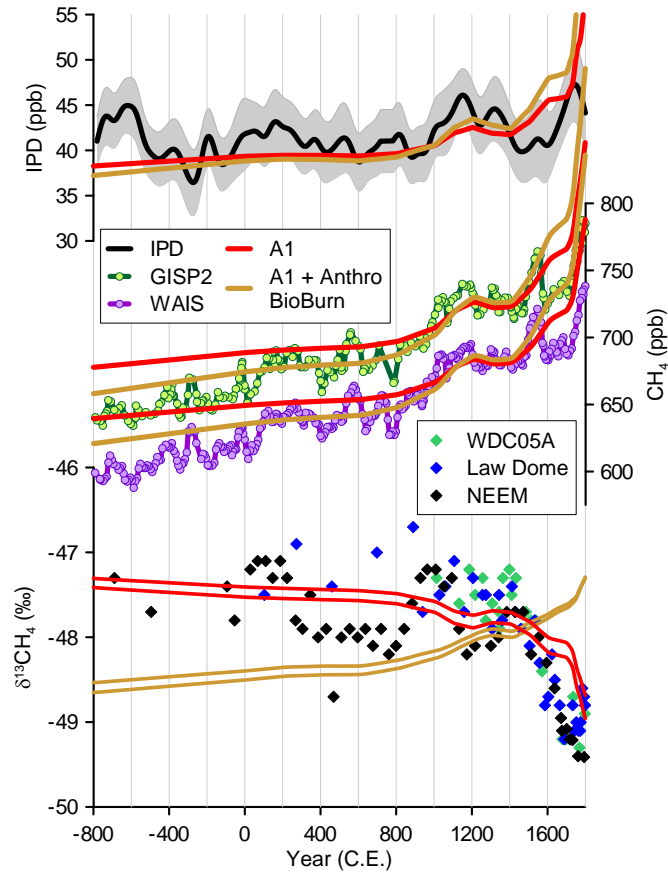


Fig. S13. Model results from Scenario A1 if per-capita scaling of anthropogenic biomass burning emissions is included. In this modified scenario natural biomass burning emissions were set to 15 Tg/yr (instead of 25 Tg/yr in the base scenario) and anthropogenic biomass burning emissions to 10 Tg/yr in the year 1500 C.E. (44) and allow the per-capita scaling technique to change emissions through time. $\delta^{13}\text{CH}_4$ data comes from WDC05A, Antarctica (51), Law Dome, Antarctica (50), and NEEM, Greenland (47).

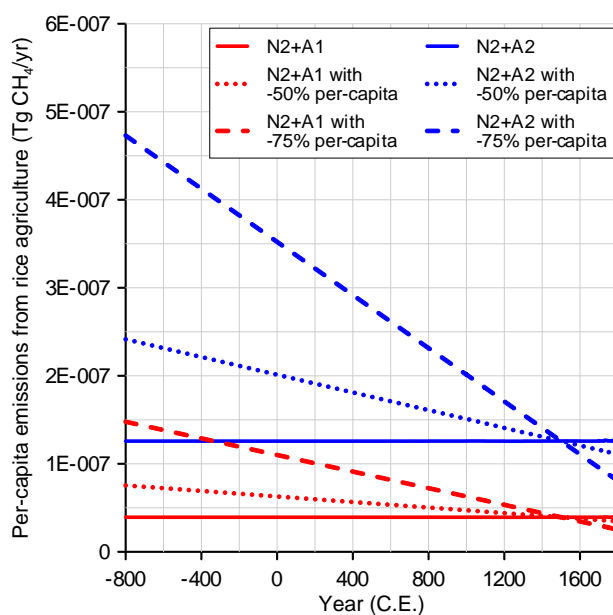


Fig. S14. Per-capita emissions of methane from rice production through time used in the model scenarios. Per-capita emissions are defined in the model at the year 1500 C.E. based on the literature estimate of rice production and the population in the rice-producing region of Asia (60-140°E and 10°S-50°N), which at 1500 C.E. was approximately 254 million people. The -50% and -75% change refers to the change in per-capita emissions between 1000 B.C.E. and 1500 C.E.

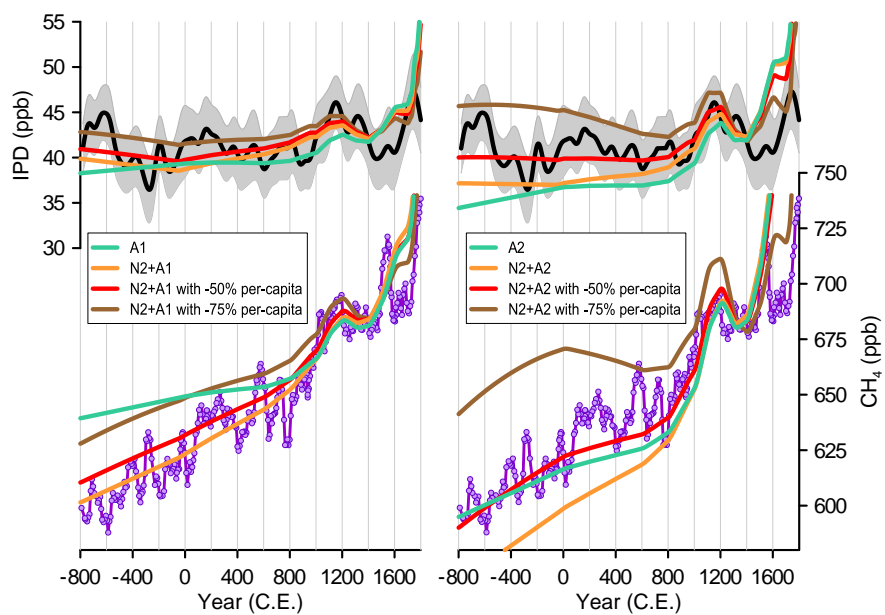


Fig. S15. Anthropogenic scenarios with a range of changes in per-capita emissions through time. Note that scenario A1 & A2 have constant natural emissions, approximately equivalent to what would be expected from N1+A1 and N1+A2 since scenario N1 contains only small changes in emissions.

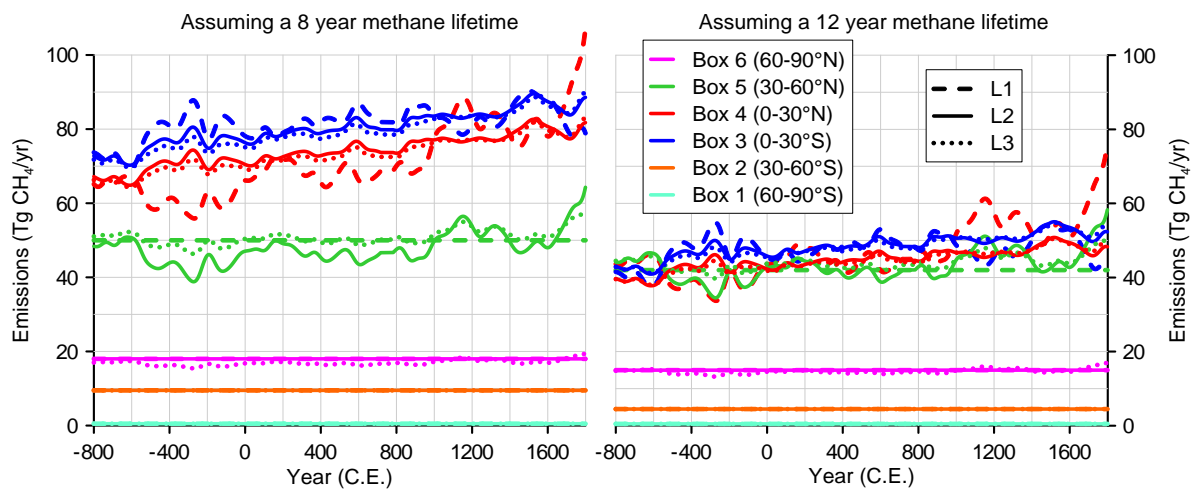


Fig. S16. Calculated emissions for scenarios L1-3 assuming a methane lifetime of 8 years (left) and 12 years (right). The change in zonal emissions is reported in Table S2.

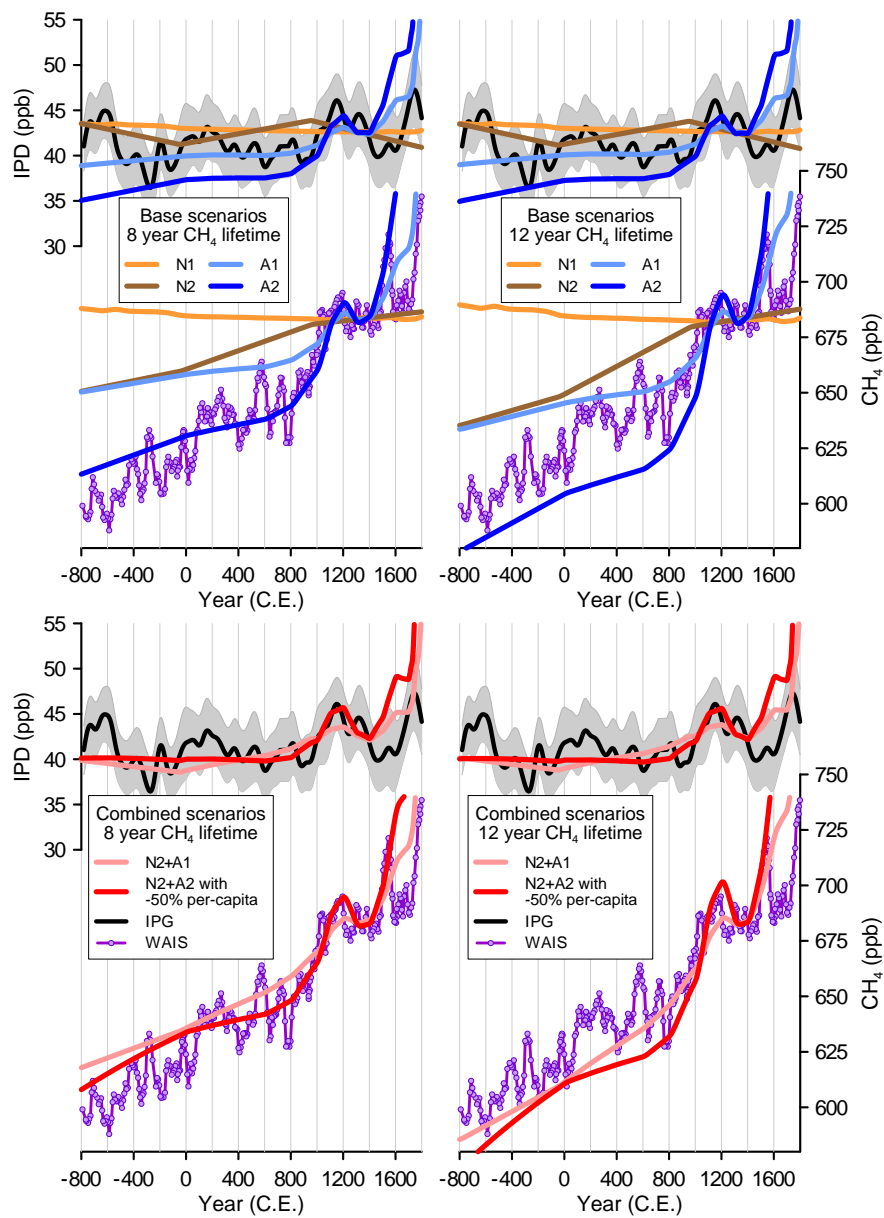


Fig. S17. Modeled methane concentrations assuming a methane lifetime of 8 years (left panels) and 12 years (right panels).

